

# Understanding and Addressing the Performance Asymmetry Issue in Semitransparent Laminated Organic Photovoltaic Devices

Gulzada Beket, Anton Zubayer, Leonie Pap, Huagui Lai, Samiran Bairagi, Nakul Jain, Jochen Stahn, Fan Fu, Kenneth Järrendahl, Fredrik Eriksson, Xabier Rodríguez-Martínez, Olle Inganäs, Uli Würfel, Thomas Österberg,\* Jonas Bergqvist, and Feng Gao\*

Organic photovoltaics (OPVs) offer a promising solution for indoor energy harvesting. However, fundamental investigations to understand and optimize industrial processes such as roll-to-roll lamination for upscaling remain limited. This study investigates a critical failure mode in the upscaling of OPVs. One major challenge for thick semitransparent laminated OPV devices is current–voltage ( $J$ – $V$ ) asymmetry, where performance under cathode-side illumination exceeds that under anode-side illumination. X-ray reflectivity, neutron reflectivity, and drift-diffusion simulations reveal that a vertically stratified polymer-rich region within the bulk of photoactive layers is the main cause of asymmetric  $J$ – $V$  characteristics. Based on this fundamental understanding, a model is proposed to explain the mechanism, wherein electron extraction is hindered by the polymer-rich region during anode illumination. By exploring upscaling-compatible blends, cathode/anode-balanced, high-performing, and air-stable semitransparent laminated OPVs are developed for indoor applications using commercially available PV-X-plus material. These findings provide valuable guidance for designing OPVs with balanced performance, facilitating roll-to-roll adoption and commercialization.

## 1. Introduction

Use of independent wireless systems and sensors for monitoring environments, both in public places and in homes, has increased significantly, leading to the rise of the Internet of Things (IoT). While batteries are the preferred power source for operating IoT devices, their use poses challenges due to the need for periodic replacement and maintenance, as well as concerns about toxicity and recycling. Exploring alternatives such as using ambient light harvesting to replace or extend the lifespan of batteries offers a sustainable solution for powering IoT devices.<sup>[1–3]</sup> Organic photovoltaics (OPVs) are an attractive choice for indoor applications due to their advantages over traditional inorganic light-harvesters, including flexibility, energy-efficient production processes, lower environmental impact and toxicity, as well as aesthetic and

G. Beket, N. Jain, O. Inganäs, F. Gao  
Department of Physics  
Chemistry and Biology (IFM)  
Division of Electronic and Photonic Materials (EFM)  
Linköping University  
Linköping 583 30, Sweden  
E-mail: [feng.gao@liu.se](mailto:feng.gao@liu.se)

G. Beket, T. Österberg, J. Bergqvist  
Epishine AB  
Attorpsgatan 2, Linköping 582 73, Sweden  
E-mail: [thomas.osterberg@epishine.com](mailto:thomas.osterberg@epishine.com)

A. Zubayer, S. Bairagi, K. Järrendahl, F. Eriksson  
Department of Physics  
Chemistry and Biology (IFM)  
Division of Thin Film Physics  
Linköping University  
Linköping 583 30, Sweden

L. Pap, U. Würfel  
Fraunhofer Institute for Solar Energy Systems ISE  
79110 Freiburg, Germany

L. Pap, U. Würfel  
Materials Research Center FMF  
University of Freiburg  
79104 Freiburg, Germany

H. Lai, F. Fu  
Laboratory for Thin Films and Photovoltaics  
Empa–Swiss Federal Laboratories for Materials Science and Technology  
Ueberlandstrasse 129, Duebendorf CH-8600, Switzerland

J. Stahn  
PSI Center for Neutron and Muon Sciences  
PSI, Villigen 5323, Switzerland

X. Rodríguez-Martínez  
Centro de Investigación en Tecnoloxías Navais e Industriais (CITENI)  
Universidade da Coruña  
Campus de Esteiro s/n, Ferrol 15403, Spain

 The ORCID identification number(s) for the author(s) of this article can be found under <https://doi.org/10.1002/adfm.202502951>

© 2025 The Author(s). Advanced Functional Materials published by Wiley-VCH GmbH. This is an open access article under the terms of the [Creative Commons Attribution](https://creativecommons.org/licenses/by/4.0/) License, which permits use, distribution and reproduction in any medium, provided the original work is properly cited.

DOI: [10.1002/adfm.202502951](https://doi.org/10.1002/adfm.202502951)

design versatility.<sup>[4,5]</sup> These features make OPVs more adaptable and easier to integrate with IoT devices, making them a well-suited power source for autonomous devices.<sup>[6,7]</sup> Moreover, the main absorption bands of light-harvesting organic molecules can be tailored to match the indoor light spectrum, optimizing the conversion of ambient light to electricity by minimizing thermalization and non-absorption losses. Given the narrow range of incident (indoor) light, the optimal bandgap for OPVs can be set between 1.8 and 2.0 eV,<sup>[8]</sup> though this may vary depending on the emission spectra of different lamps. While newly developed non-fullerene acceptor (NFA) based OPVs have demonstrated impressive efficiencies at the laboratory scale,<sup>[9,10]</sup> they have yet to meet the criteria for successful roll-to-roll (R2R) upscaling before reaching commercial impact in the IoT market.<sup>[11,12]</sup>

One manufacturing technique that aligns with industrialization requirements is the lamination of the active layer on a semitransparent anode with the same active layer on a semitransparent cathode, resulting in a fully functional indoor OPV (IOPV) device<sup>[13,14]</sup> (see **Figure 1a**). The primary advantages of lamination include elimination of vacuum-based processing for the front and back electrodes, which typically demands high energy input. For IOPV devices, the strict conductivity demands of outdoor photovoltaics are relaxed, allowing poly(3,4-ethylenedioxythiophene)-poly(styrenesulfonate) (PEDOT: PSS) to function effectively as semitransparent electrodes in the laminated IOPV architecture. Furthermore, since IOPVs are more sensitive to shunt resistance than to series resistance, lamination offers an additional benefit by enhancing shunt resistance. This is attributed to the reduced formation of shunting pathways, which often arise from defects and pinholes introduced during solution-based processing.<sup>[13]</sup> Thus, lamination supports a more robust manufacturing process with fewer low-performing outliers caused by shunting defects. One critical factor contributing to the upscaling challenge is the predominant focus of research on highly efficient materials utilizing p-type layer–intrinsic photoactive layer–n-type layer (p-i-n) structure, whereas n-i-p structure is found to be more suitable for upscaling efforts.<sup>[15]</sup> As in laminated devices the cathode side mimics the inverted n-i-p structure and the anode side the conventional p-i-n structure with metal-capped electrodes,<sup>[16]</sup> laminated OPV devices offer a valuable opportunity to explore and understand both device structures simultaneously, without excessive time and material utilization.

Despite these advantages, laminated devices face the challenge of performance asymmetry when illuminated from different sides. For example, Bergqvist et al. discovered that in laminated devices using PEDOT:PSS as electrodes, the anode side of fullerene-based devices degrades upon air exposure, leading to reduced photocurrent extraction under anode-side illumination.<sup>[13]</sup> Similarly, Rodríguez-Martínez et al. attributed the performance asymmetry to a filtering layer within the photoactive layer (PAL) of PM6 (poly[(2,6-(4,8-bis(5-(2-ethylhexyl-3-fluoro)thiophen-2-yl)-benzo[1,2-b:4,5-b']dithiophene))-alt-(5,5-(1',3'-di-2-thienyl-5',7'-bis(2-ethylhexyl)benzo[1',2'-c:4',5'-c']dithiophene-4,8-dione))]: IO-4Cl (3,9-bis[5,6-dichloro-1H-indene-1,3(2H)dione]-5,5,11,11-tetrakis(4-hexylphenyl)-dithieno[2,3-d:2',3'-d']-s-indaceno[1,2-b:5,6-b']dithiophene (PM6:IO-4Cl), which does not contribute to the photocurrent.<sup>[14]</sup> The authors speculated that this effect

originated from inherent properties of the blend, such as morphology and wettability. Interestingly, the effect was observed regardless of whether processing occurred in ambient or inert conditions. While they suggested mitigating the performance asymmetry issue by using thinner photoactive layers, such an approach contradicts the goal of scalable R2R coating. Notably, R2R printing techniques require OPVs with PAL thicknesses exceeding 200 nm to enhance production yield by reducing defect density.<sup>[17,18]</sup> Thus, there is a need for thick PALs that can tolerate thickness variations while enabling control over film morphology, especially at greater thicknesses. While some studies focus on controlling the bulk morphology of thick PALs,<sup>[19,20]</sup> further research is needed to explore the relationship between thick PALs and vertical phase distribution to address this challenge.

This study provides an in-depth understanding of the performance asymmetry in laminated OPV devices using reflectivity techniques, specifically X-ray reflectivity (XRR) and neutron reflectivity (NR). Through a combination of experimental investigations and drift-diffusion simulations, we reveal that the cathode/anode electrical asymmetry in semitransparent laminated devices results from the unfavorable vertical distribution of the donor and acceptor materials within thick PALs, i.e., thick vertically stratified polymer-rich regions at the lamination interfaces. This region acts as a charge-selective energetic barrier, hindering the extraction of electrons traveling through the polymer-rich region on their way to the cathode, i.e., those generated closer to the anode, resulting in performance asymmetry with respect to the illumination direction. Investigations into the causes of vertical stratification on the cathode PAL reveal an interplay of thermodynamic factors, predominantly driven by surface-free energy variations across different material interfaces and processing conditions. We find that the commercially available PV-X Plus<sup>[21]</sup> blend not only demonstrates high indoor performance but also exhibits symmetric *J*–*V* characteristics, attributed to their much-decreased segregated region (down to 10 nm). Our results provide a fundamental understanding of a long-standing challenge in laminated OPV devices and further demonstrate that this issue is not inherent to lamination technology itself. Instead, it can be mitigated by considering thermodynamic properties and drying kinetics, paving the way for semitransparent indoor OPVs for R2R adoption.

## 2. Results and Discussion

### 2.1. Vertical Stratification of Photoactive Layers

This study focuses on semitransparent laminated IOPV devices, where PEDOT:PSS serves as both the anode and cathode electrode, with SnO<sub>2</sub> as the electron transport layer (ETL) and fullerene-based (PBTZT-stat-BDIT:[6,6]-phenyl-C<sub>61</sub>-butyric acid methyl ester (PC<sub>61</sub>BM)) and NFA-based (PM6:IO-4Cl) blends as archetypal OPV PALs. These two PALs are purposefully targeted for ambient light harvesting, as they present high bandgap, having absorption onset optimized for typical indoor irradiances.<sup>[9,22]</sup> The energy level diagrams of the components are presented in **Figure 1b**, while the chemical structures of the PAL materials in **Figure 1c,d**. The cathode and anode stacks are processed independently on polyethylene terephthalate (PET) substrates. The

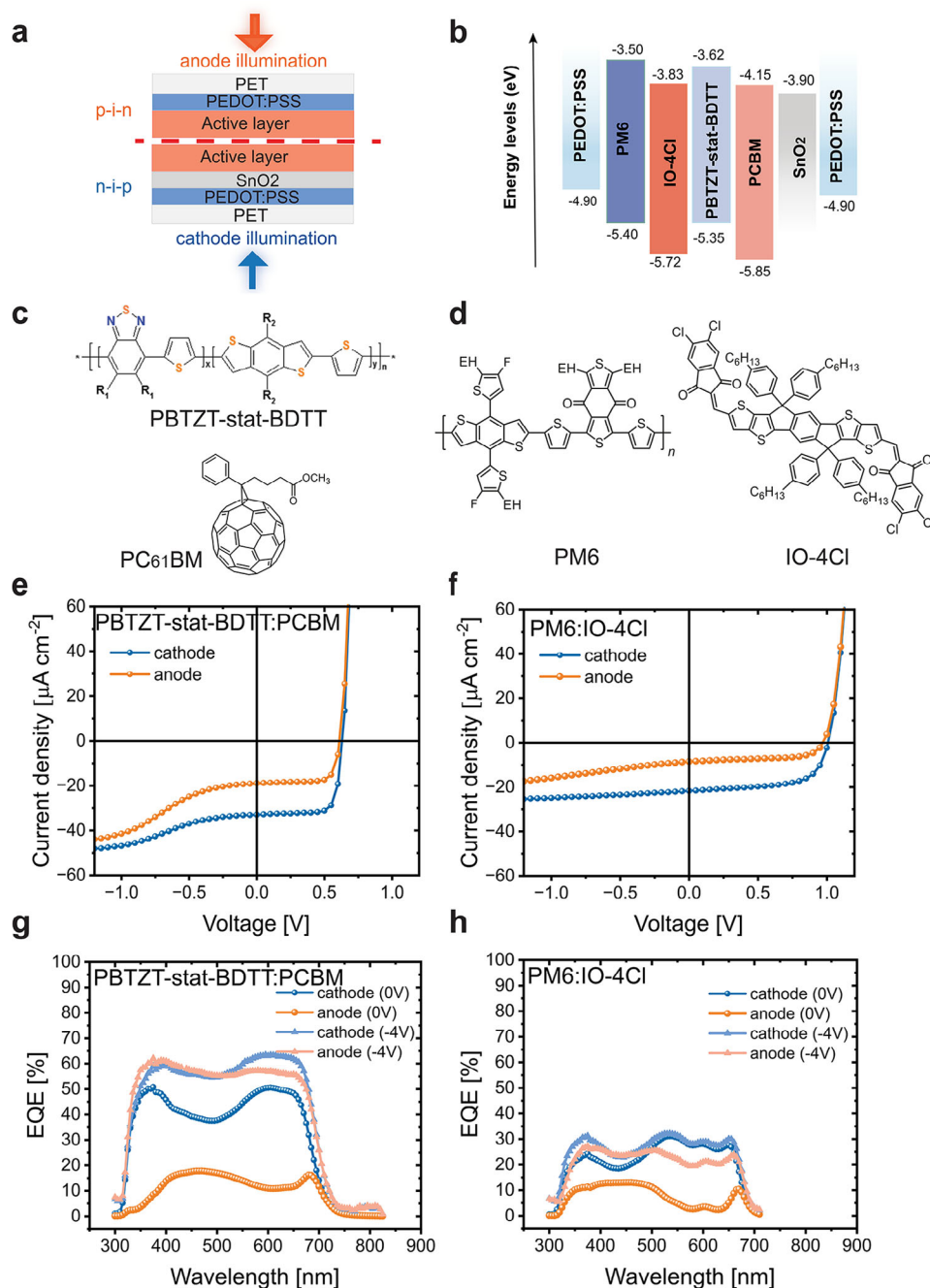


**Figure 1.** a) Schematic of the laminated indoor OPV stack, illuminated either through cathode (blue arrow) or anode (orange arrow) electrode. b) Energy diagram represents the HOMO and LUMO levels of PM6 and IO-4Cl as well as PBTZT-stat-BDTT and PC<sub>61</sub>BM,<sup>[9,22]</sup> and the work functions of the PEDOT:PSS electrodes and SnO<sub>2</sub> interlayer (obtained from the commercial suppliers). Molecular structures of the photoactive layers c) PBTZT-stat-BDTT:PC<sub>61</sub>BM and d) PM6:IO-4Cl. Typical *J*-*V* curves of e) 330 nm PBTZT-stat-BDTT:PC<sub>61</sub>BM and f) 220 nm PM6:IO-4Cl based IOPV devices illuminated either through the cathode or anode side. EQE spectrum of g) 330 nm PBTZT-stat-BDTT:PC<sub>61</sub>BM and h) 220 nm PM6:IO-4Cl based IOPV devices illuminated either through cathode or anode side at short circuit (0 V) and under reverse bias (-4 V).

processed cathode and anode sides are brought together in between two counter-rotating lamination rolls to assemble them under inert conditions. A schematic of the laminated indoor OPV device structure is shown in Figure 1a. The anode side of the laminated device resembles the typical p-i-n OPV structure, while

cathode side resembles the n-i-p OPV structure. The experiments are carried out in a fully inert atmosphere to avoid potential degradation or increased trap density induced by the presence of ambient air and light during ambient processing.<sup>[23,24]</sup> The devices are characterized under a typical indoor 500 lux 4000 K LED

illumination (with the spectral irradiance shown in Figure S1, Supporting Information). These active layers exhibit asymmetric  $J$ - $V$  characteristics depending on the illumination side when assembled as semitransparent laminated devices.

Typical asymmetric  $J$ - $V$  curves and PV figures-of-merit of PBTZT-stat-BDTP:PC<sub>61</sub>BM and PM6:IO-4Cl based IOPV devices under 500 lux are shown in Figure 1e,f, and Table S1 (Supporting Information), respectively. For both PALs, there is a slight difference in open-circuit voltage ( $V_{oc}$ ) depending on the illumination side. The major reduction is from short-circuit current density ( $J_{sc}$ ) for anode illuminated devices in both cases, with the PM6:IO-4Cl based devices also showing slight difference in fill factor ( $FF$ ). For PBTZT-stat-BDTP:PC<sub>61</sub>BM based devices,  $J_{sc}$  of 33  $\mu\text{A cm}^{-2}$  is obtained under cathode illumination, while anode illumination results in  $J_{sc}$  of 19  $\mu\text{A cm}^{-2}$ . Similar electrical asymmetry is observed for PM6:IO-4Cl based devices, with  $J_{sc}$  of 24  $\mu\text{A cm}^{-2}$  under cathode illumination and 7  $\mu\text{A cm}^{-2}$  under anode illumination. To gain further insights into the  $J_{sc}$  asymmetry in the IOPV devices, we measured external quantum efficiency ( $EQE$ ) spectra at short circuits (0 V) and under reverse bias (-4 V). Figure 1g,h illustrates that in both cases  $EQE$  values are reduced significantly during anode illumination compared to cathode illumination at the short-circuit condition. Under reverse bias, both the cathode and anode sides show increased  $EQE$ , with a more significant enhancement observed for anode illumination. This leads to a more balanced  $EQE$  spectrum. These findings align with the  $J$ - $V$  characteristics, indicating complete photocurrent extraction at sufficient reverse bias. A similar  $J$ - $V$  behavior was also found in previous reports,<sup>[14]</sup> where the existence of a filtering layer was proposed. The filtering layer was argued to absorb light without contributing to photocurrent, even when devices were fully processed in inert conditions; however, a mechanistic explanation for this phenomenon remains unresolved. These observations raise questions about how the structural and compositional variations within the PALs may drive the observed photoelectrical asymmetry.

To investigate the vertical composition of PALs in our device architecture, we employ a combination of X-ray Reflectivity (XRR) and Neutron Reflectivity (NR) measurements on both cathode and anode stacks prior to the lamination process. These non-destructive, high-resolution methods probe the depth-dependent scattering length density (SLD) of thin films, enabling quantitative analysis of vertical phase distribution, layer thickness, interface roughness, and compositional gradients across multilayer stacks. Unlike conventional profiling methods, which require sputtering or etching, reflectivity methods preserve the integrity of the sample and are particularly well suited to soft-matter systems.<sup>[25]</sup> By measuring the intensity of specularly reflected X-rays or neutrons as a function of momentum transfer ( $q$ ), we obtain reflectivity curves that are sensitive to variations in electron density (XRR) or nuclear scattering length density (NR) along the film normal. These reflectivity profiles are analyzed by comparing experimental data to simulated curves generated from a multilayer model, which describes the film as a series of discrete layers with defined physical and geometrical parameters. Fitting was performed using the GenX<sup>[26]</sup> software package (see Supporting Information), yielding model-derived SLD profiles that describe material density as a function of depth. For the PAL blends, the SLD profiles reveal vertical stratification and varia-

tions in layer organization based on deposition onto cathode versus anode stacks.

To convert the measured reflectivity curves into SLD profiles, we constructed and fitted both single-layer and two-layer models. A single-layer model was used to describe interlayers, electrodes, and the PAL deposited on the anode stack, where the composition appeared relatively uniform. In contrast, for PALs deposited on the cathode stack, both single- and two-layer models were applied to evaluate the potential presence of vertical stratification. Inhomogeneous layers were modeled by dividing them into sublayers with varying SLDs. The two-layer model is particularly flexible, as it can capture vertical stratification when the sublayers differ in SLD or approximate a homogeneous layer when the sublayers share similar SLD values. For completeness, the single-layer fits are provided in the Supporting Information.

Building on this approach, we investigate the vertical density distribution of cathode (PEDOT:PSS/SnO<sub>2</sub>/PAL) and anode (PEDOT:PSS/PAL) stacks with PBTZT-stat-BDTP:PC<sub>61</sub>BM and PM6:IO-4Cl PALs. These stacks were processed independently and analyzed via XRR measurements. While derived SLD depth profiles for the cathode half-stacks (Figure S2, Supporting Information) show reasonable fits with single-layer models, two-layer models more accurately reveal vertical stratification within the PALs. The XRR fits for the two-layer models (Figure S3, Supporting Information), along with the derived SLD depth profiles in Figure 2a,b, reveal differences in SLD at the PAL surface, indicating stratification. Fitted SLDs of PEDOT:PSS, SnO<sub>2</sub>, PBTZT-stat-BDTP:PC<sub>61</sub>BM and PM6:IO-4Cl are found to be  $0.40 \times 10^{-6}$ ,  $0.87 \times 10^{-6}$ ,  $0.35$ - $0.42 \times 10^{-6}$ , and  $0.35$ - $0.45 \times 10^{-6} \text{ \AA}^{-2}$ , respectively. At  $\approx 30$  nm from the surface SLD (air interface) of the PBTZT-stat-BDTP:PC<sub>61</sub>BM PAL on the cathode stack, there is a distinct difference in SLD compared to the bulk of the bulk heterojunction (BHJ) PAL, suggesting vertical stratification of the PAL. This is different from the PAL film on the anode stack, which is homogeneously distributed on the PEDOT:PSS electrode. For the PM6:IO-4Cl PAL, we observe a similarity: there is an  $\approx 28$ -nm-thick, vertically stratified region at the surface of the 110 nm PAL on the cathode side. In contrast, the anode stack of PM6:IO-4Cl shows a homogeneous 110 nm distribution on the PEDOT:PSS electrode. To complement the XRR results, we also conducted NR measurements, which provide better depth sensitivity, especially for light elements in organic semiconductor materials. The 30 nm vertical stratification observed in XRR results is confirmed by the NR measurements, with the PM6:IO-4Cl PAL deposited on both cathode and anode stacks as an example (Figure S4, Supporting Information). Moreover, the sharp interfaces between layers observed in XRR and NR results indicate the absence of interfacial degradation or diffusion in the laminated device architecture, in contrast to the effects reported for devices with evaporated top electrodes.<sup>[27]</sup>

To gain deeper insight into the vertically stratified region, we conducted Time-of-Flight Secondary Ion Mass Spectrometry (ToF-SIMS) on a PM6:IO-4Cl film deposited on a Si/SiO<sub>x</sub> substrate, allowing us to resolve the vertical atomic distribution within the PAL (Figure S5, Supporting Information). The Cl<sup>-</sup> signal, which is solely attributed to the IO-4Cl acceptor, was notably reduced at the surface of the film, indicating that the polymer donor content is higher than the acceptor content at the film surface. To further validate the segregation of a polymer-rich

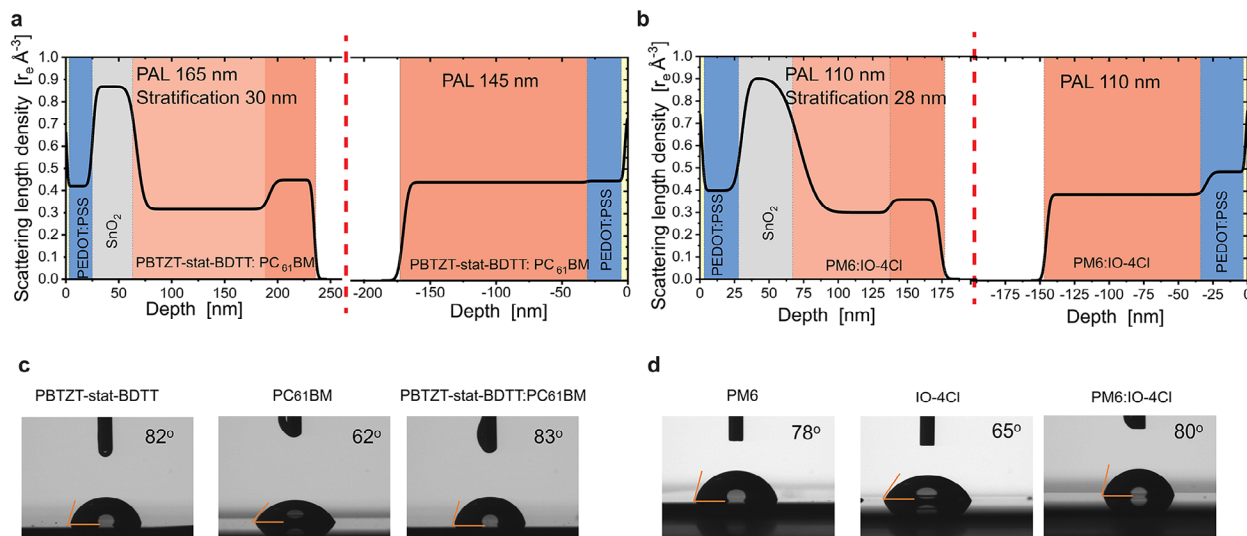


**Figure 2.** Scattering length density (SLD) depth profiles of a) PBTZT-stat-BDTT:PC<sub>61</sub>BM and b) PM6:IO-4Cl films on PEDOT:PSS/SnO<sub>2</sub> cathodes and PEDOT:PSS anodes, mimicking the device architecture. Contact angle measurements of c) neat PBTZT-stat-BDTT, PC<sub>61</sub>BM, and PBTZT-stat-BDTT:PC<sub>61</sub>BM blend films, and d) neat PM6, IO-4Cl, and PM6:IO-4Cl blend films on Si/SiO<sub>x</sub> substrates using ethylene glycol (EG) as a probing solvent.

region at the top surface of the BHJ, we examined the surface energies of the PAL films on Si/SiO<sub>x</sub> substrate using contact angle (CA) measurements. We used three different solvents: ethylene glycol (Figure 2c,d), deionized water, and diiodomethane (Figure S6, Supporting Information). We calculated the surface energy of pure donor and acceptor films, and their respective BHJ blends using Owens-Wendt and Fowkes methods.<sup>[28–30]</sup> The results for each method are in Table S2 (Supporting Information). Given the close agreement between the results from both methods, an average value was calculated for each set of measurements. This approach provides a unified estimate of the surface energy for each case, giving more comprehensive understanding while accounting for slight variations between methods. The corresponding surface energies are as follows:  $\gamma$ (PBTZT-stat-BDTT) = 26.5 mN m<sup>-1</sup>,  $\gamma$ (PC<sub>61</sub>BM) = 47 mN m<sup>-1</sup>, and  $\gamma$ (PBTZT-stat-BDTT:PC<sub>61</sub>BM) = 25 mN m<sup>-1</sup> for one system, and  $\gamma$ (PM6) = 32.5 mN m<sup>-1</sup>,  $\gamma$ (IO-4Cl) = 44 mN m<sup>-1</sup>, and  $\gamma$ (PM6:IO-4Cl) = 31 mN m<sup>-1</sup> for the other. The surface energies of the pure donor polymer films in both systems closely match those of the corresponding PAL blend films, whereas the surface energies of the pure acceptor films differ significantly. This suggests that the surfaces of both BHJ films are enriched with their respective donor polymers.

These complementary studies, NR, ToF-SIMS, and CA, consistently strengthen the XRR observations, confirming that the top surface of the blend film in both active layers is enriched with polymer. The electrical consequences of this polymer enrichment at the top surface are the key driver of the asymmetric  $J$ - $V$  curves detailed in the following sections.

## 2.2. Electrical Modelling and Mechanism of Asymmetric $J$ - $V$ Characteristics

Having established the presence of vertical stratification within the bulk of the PAL, we now investigate its influence on the elec-

trical properties of laminated IOPV devices. In particular, we investigate how this affects extraction of photogenerated charge carriers in the PBTZT-stat-BDTT:PC<sub>61</sub>BM PAL. To accomplish this, we conducted drift-diffusion simulations on a semitransparent IOPV device, where the cathode PAL is laminated onto the anode PAL as per experiments. The optical constants used to calculate the charge carrier generation profile are shown in Figure S7 (Supporting Information), with the resulting generation profile presented in Figure S8 (Supporting Information). Energy level values are provided in Figures S9 and S10 (Supporting Information).

The model schematic for the drift-diffusion simulations is shown in Figure 3a, where a vertically stratified donor polymer-rich region is positioned between two BHJ PALs at the lamination interface. This stratified region was initially modeled as an electron injection barrier at the lamination interface, with the corresponding electrical parameters provided in Table S3 (Supporting Information). The height of the electron injection barrier  $\Delta_{LL} = E_{LUMO,D} - E_{LUMO,A}$  is varied from 0 to -0.40 eV. The results in Figure 3 demonstrate that this injection barrier can indeed cause asymmetry in the  $J$ - $V$  characteristics under cathode and anode illumination, closely resembling the experimental observations. Both cathode-illumination (Figure 3b) and anode-illumination (Figure 3c)  $J$ - $V$  curves are affected by the barrier height, with the current densities more significantly affected for the anode-illumination case. The experimental  $J$ - $V$  curves are best matched with an electron injection barrier in the range of -0.30 to -0.35 eV. To further understand the impact of the energetic barrier, Figure S11 (Supporting Information) provides a detailed analysis of electron and hole densities, as well as bimolecular recombination, across the PAL at 0 V (short-circuit condition). Considering an energetic barrier of -0.31 eV for both illumination directions, it is observed that for anode illumination there is significant accumulation of electrons (blue solid line) directly in front of the energetic barrier mimicking the interface between BHJ and pure donor layer. Due to the corresponding built-up of

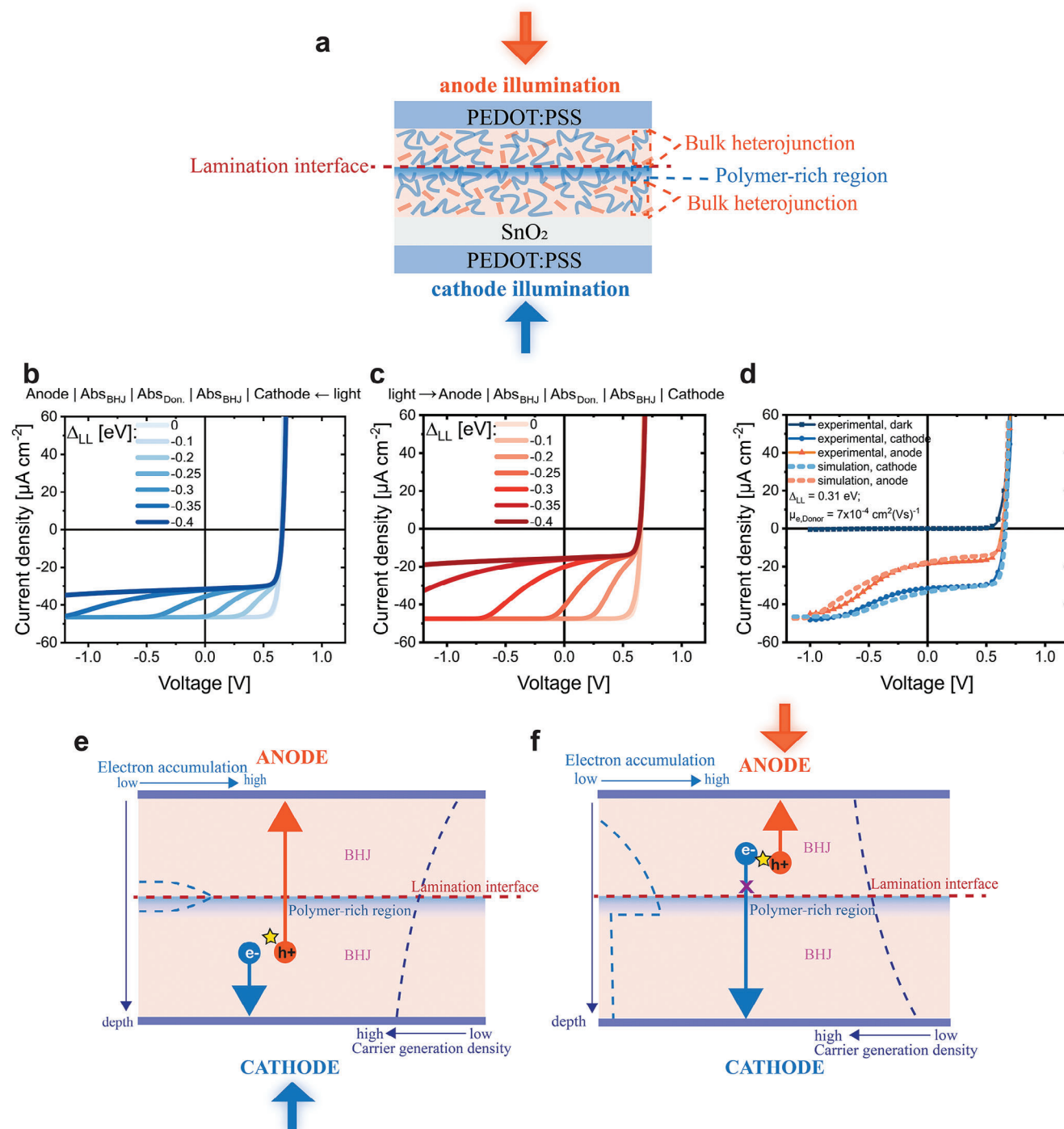


**Figure 3.** a) Schematic model used for electrical simulations. Drift-diffusion simulations show that setting the polymer-rich region as an injection barrier at the lamination interface leads to an s-kink evolution in the  $J$ - $V$  curves with increasing barrier height under b) cathode illumination and c) anode illumination. Note the significantly reduced  $J_{sc}$  during anode illumination compared to cathode illumination. d) Drift-diffusion simulations illustrate the polymer-rich region as an area with reduced electron mobility and an energetic barrier of  $-0.31$  eV. The combination of the introduced injection barrier and reduced electron mobility within the polymer-rich region best replicates the experimental results. Proposed model explaining  $J$ - $V$  asymmetry in semitransparent laminated OPVs under e) cathode and f) anode illumination.

space charge, also the concentration of holes is higher. Together, this leads to a substantial increase of bimolecular recombination in this region compared to the case of cathode illumination.

For a zero energetic barrier, variations in electron mobility ( $\mu_e$ ) between  $10^{-3}$  and  $2 \times 10^{-8}$   $\text{cm}^2$   $(\text{Vs})^{-1}$ , within the polymer-rich region can also induce  $J$ - $V$  asymmetry (Figure S12, Supporting Information). The effect of reduced  $\mu_e$  is again more pronounced under anode illumination, leading to a reduced  $J_{sc}$ , as holes can be readily extracted at the closer anode contact. Similar to the case of the energetic barrier, poor electron transport through the stratified donor-rich region causes accumulation, increasing bimolecular recombination. To explore this further, we varied both the electron mobility and the energetic barrier height in the polymer-rich, vertically stratified region, see Figure 3d. Our findings demonstrate that adjusting both simulation parameters closely aligns with the experimental results, effectively replicating the reduced performance, particularly in the extracted photocurrent under anode illumination. Notably, a barrier height of  $-0.31$  eV and electron mobility of  $7 \times 10^{-4}$   $\text{cm}^2$   $(\text{Vs})^{-1}$ , successfully reproduce the observed  $J$ - $V$  asymmetry.

Based on experimental and simulation outcomes, we propose a model for the  $J$ - $V$  asymmetry observed in semitransparent laminated IOPVs. During cathode illumination as in Figure 3e, charge generation follows rather an exponential decay function thus it predominantly occurs near the cathode contact. In this case, charge extraction remains much less affected by the polymer-rich region at the lamination interface because most electrons are readily extracted at the nearby cathode contact. Despite the long distance traveled, holes are efficiently extracted at the anode contact as they do not encounter any energetic barrier. In contrast, during anode illumination (Figure 3f), while holes generated close to the anode contact are readily extracted, a significant fraction of the photogenerated electrons encounter the polymer-rich region on their way to the cathode contact, hindering their extraction. We show that electrons from the anode side accumulate near the polymer-rich barrier region, creating an unusual mid-device electric field.

In general, it can be stated that the unbalanced charge extraction in such devices leads to the observed asymmetric  $J$ - $V$  characteristics. The extent of this asymmetry is highly sensitive to the fraction of electrons encountering significant hindrance on their way to the cathode contact. This hindrance is much more pronounced under anode illumination. Such a hindrance can arise from an energetic barrier, a region with poor transport properties (i.e., strongly reduced electron mobility), or a combination of both.

### 2.3. Factors Affecting Vertical Stratification in Laminated IOPV Devices

The vertical distribution of BHJ blends is a complex process influenced by thermodynamic principles and drying kinetics factors.<sup>[25,31,32]</sup> We find that the underlying factors contributing to the formation of vertical stratification within the PALs, include processing conditions, such as solvent choice, interlayer surface properties, and miscibility between components.

In our efforts to understand this phenomenon, we conducted a comparative study of solvents employed in the processing of

PBTZT-stat-BDIT:PC<sub>61</sub>BM PAL system. Our investigation revealed that 1-Methylnaphthalene, an additive solvent utilized for enhancing device performance, induces asymmetric behavior in OPV devices as can be seen in Figure S13 (Supporting Information). We found that removing 1-Methylnaphthalene from the o-xylene based ink eliminates vertical stratification, resulting in a homogeneous vertical distribution (Figure S14, Supporting Information). The surface energy value of the blend processed from o-xylene and additive 1-Methylnaphthalene with asymmetric  $J$ - $V$  characteristics is similar to that of the polymer donor material (Table S4, Supporting Information), suggesting polymer accumulation at the top surface. In contrast, when the blend is processed using only o-xylene solvent, the surface energy value is calculated to be an approximate average of the pure polymer donor and fullerene acceptor materials surface energies. Owing to its higher boiling point<sup>[33]</sup> compared to o-xylene (144 °C), 1-Methylnaphthalene (240–243 °C) extends the drying transient over a significantly prolonged timescale. The distinct solvation characteristics of 1-Methylnaphthalene compared to o-xylene, combined with the extended drying process, might give the system a different duration for equilibration.

Furthermore, based on previous XRR results, we learned that surface energy of underlying layer influences the vertical distribution of PALs, i.e., PALs deposited on SnO<sub>2</sub> ETL result in vertical stratification compared to PALs deposited on PEDOT:PSS. Therefore, the interlayer beneath the PAL also plays a significant role in its vertical stratification.

The miscibility of the donor-acceptor binary blend is another factor that affects vertical stratification. We calculated the Flory-Huggins interaction parameter ( $\chi$ )<sup>[34–36]</sup> for each blend system (Table S2, Supporting Information) using the following formula  $\chi = (\sqrt{\gamma_D} - \sqrt{\gamma_A})^2$ . For the PBTZT-stat-BDIT:PC<sub>61</sub>BM blend, the interaction parameter  $\chi$  is 2.34 and 3.61 based on surface energy values calculated using the Owens-Wendt and Fowkes methods, respectively, suggesting poor miscibility between the components. From a thermodynamic perspective, good miscibility between donor and acceptor compounds in BHJ tends to promote a more homogeneous distribution of these materials throughout the PAL. In addition to this fullerene-based system, we also examined PAL PM6:PC<sub>61</sub>BM blend miscibility. Considering the surface energy values of PM6 and PC<sub>61</sub>BM, we calculate the Flory-Huggins interaction parameter ( $\chi$ ) for the PM6:PC<sub>61</sub>BM blend using both the Owens-Wendt and Fowkes methods. The calculated values are 0.94 and 1.77, respectively, indicating a lower  $\chi$  value, which suggests higher miscibility between the polymer and fullerene. This high miscibility results in a more homogeneous vertical distribution, as confirmed by the reflectivity measurements, which show a uniform composition profile of PAL on the cathode stack (Figure S15, Supporting Information). These results further emphasize how miscibility impacts vertical stratification in the active layer.

### 2.4. IOPV Devices with Symmetric $J$ - $V$ Characteristics

In order to identify PALs with balanced  $J$ - $V$  curves, we conducted thorough screening of several PAL BHJ-based IOPVs. Among the candidates, the commercially available ternary PV-X-plus, composed of the polymer donor PV2300, the small molecule acceptor

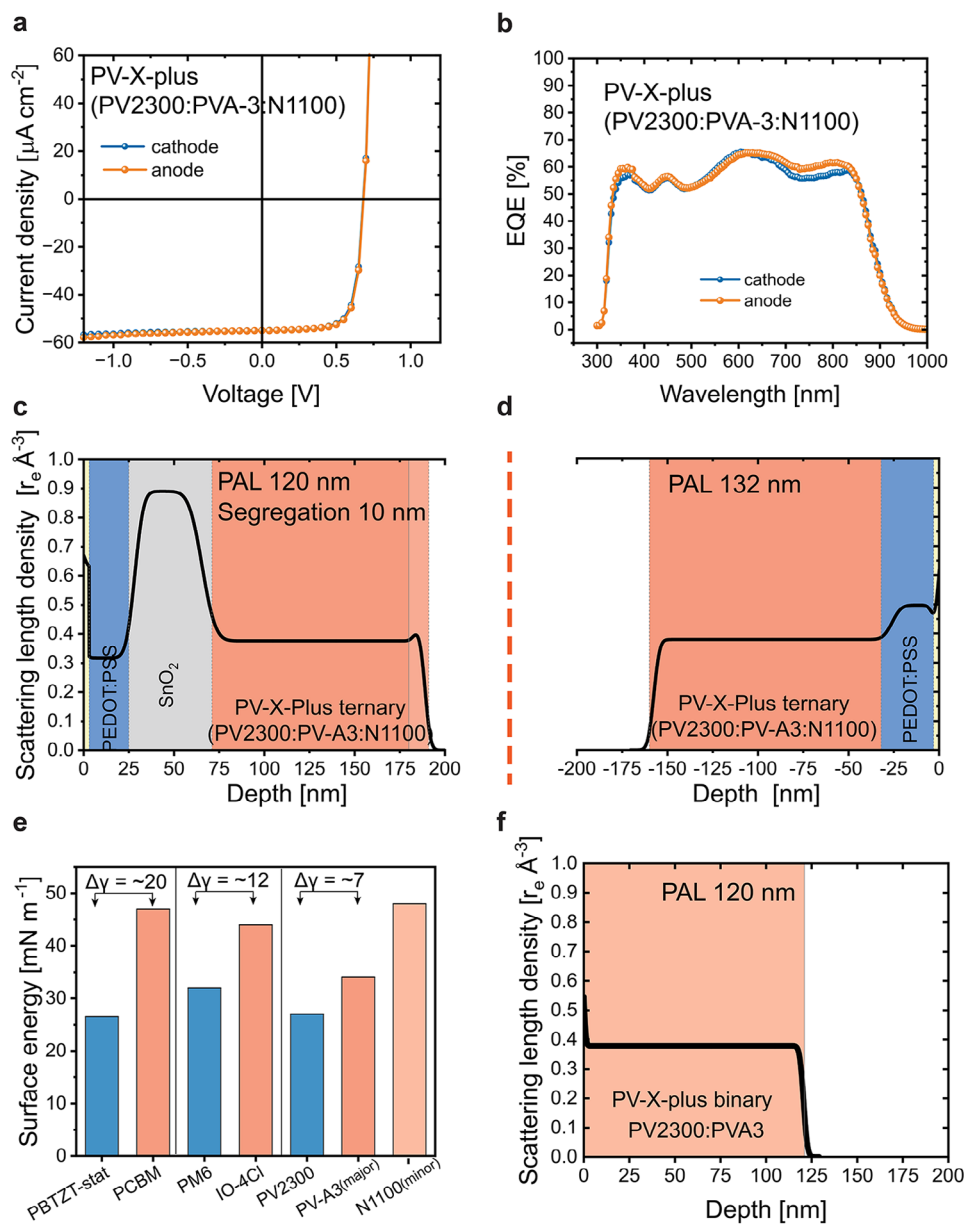


**Figure 4.** a)  $J-V$  curve and b) EQE spectrum of 260 nm thick PV-X-plus PAL-based devices illuminated either through cathode or anode side. Corresponding SLD depth profiles of the ternary PV-X-plus blend c) on the PEDOT:PSS/SnO<sub>2</sub> cathode and d) on the PEDOT:PSS anode. e) Surface energy values of donor and acceptor components used in this work. The binary mix PV2300:PV-A3 (the base of the PV-X-plus) shows a smaller surface energy difference between the two main components, favoring good miscibility and homogeneous distribution. The ternary blend PV-X-plus incorporates a minor third component, N1100, which introduces a larger surface energy mismatch that can promote vertical stratification. f) SLD depth profile of the binary PV2300:PV-A3 blend at 120 nm thickness (measured on Si/SiO<sub>x</sub> substrates), confirming a homogeneous vertical composition.

PV-A3, and a small amount of N1100 as a solid additive, stood out by demonstrating not only high indoor performance in the laminated device structure ( $V_{oc} = 0.68$  V,  $J_{sc} = 55 \mu\text{A cm}^{-2}$ ,  $FF = 0.74$ , output power density ( $P_{out}$ ) =  $27.7 \mu\text{W cm}^{-2}$  and power conversion efficiency (PCE) = 18% under 500 lux), but also highly symmetric  $J-V$  curves and balanced EQE spectra, independent of the illumination direction (Figure 4a,b).

To evaluate the trade-off between transparency and power generation, we quantified the average visible transmittance (AVT) and calculated the corresponding light utilization efficiency

(LUE) for each system (Figure S16 and Table S5, Supporting Information). PV-X-plus based IOPV devices achieved the highest AVT of 17.1% and an LUE of 3.1%, indicating the most favorable balance among the tested systems. In comparison, PBTZT-stat-BDTT:PC<sub>61</sub>BM based devices showed an AVT of 9.4% and an LUE of 1.0%, while PM6:IO-4Cl based devices exhibited a significantly lower AVT of 2.3% and LUE of 0.2%.

To simulate real-world R2R ambient processing, we exposed the half stacks of the device to air under 300 lux 4000 K LED indoor light for 15 min to investigate the effect of ambient air on

device performance and symmetry under cathode/anode illumination as shown in Figure S17 (Supporting Information). Previous studies<sup>[13]</sup> suggest that the  $J$ - $V$  asymmetry develops with air exposure for certain PAL systems, resulting in creation of electron traps at the lamination interface, further reducing electron extraction. However, we found that unlike other PALs, the PV-X-plus devices maintain  $J$ - $V$  symmetry even after air exposure. This indicates that the PV-X-plus system is highly compatible with ambient R2R processing of laminated OPVs for indoor applications.

The vertical distribution of the system on cathode and anode stacks was investigated using XRR measurements (Figure S18 and S19, Supporting Information). To construct the SLD profile of the ternary PV-X-Plus PAL on the cathode, both two-layer and one-layer models were applied. The two-layer model reveals that only the top  $\approx 10$  nm of the 120 nm cathode PAL is vertically stratified (Figure 4c). This is significantly less than the 30 nm stratified region observed in the PBTZT-stat-BDTP:PC<sub>61</sub>BM cathode PAL and 28 nm in PM6:IO-4Cl cathode PAL, both of which exhibit asymmetric  $J$ - $V$  characteristics. Notably, the SLD value within this stratified region closely matches that of the bulk material, suggesting that, based on the fitting results, the BHJ could also be interpreted as largely homogeneous. Additionally, the depth profile of the system on the anode electrode shows a homogeneous vertical distribution (Figure 4d). These findings indicate that the vertical arrangement of this system is predominantly insensitive to the interlayer interface, offering flexibility to explore different device structures without compromising performance.

To investigate the less segregation observed in the PV-X-plus system, we first examined the miscibility of its components, since thermodynamically driven phase separation is closely tied to donor-acceptor miscibility. As shown in Figure 4e, the binary PV2300:PV-A3 system (the major donor and acceptor in PV-X-plus) shows a small surface energy difference ( $\Delta\gamma \approx 7$  mN m<sup>-1</sup>), indicating good miscibility (Flory-Huggins  $\chi \approx 0.40$ ) and favorable intermixing, especially when compared to the PBTZT-stat-BDTP:PC<sub>61</sub>BM and PM6:IO-4Cl blends. This is consistent with the homogeneous vertical phase distribution observed in the SLD profile of the binary film, which remains uniform across a 120 nm thickness with no signs of vertical stratification (see Figure 4f and XRR fitting in Figure S20, Supporting Information). In contrast, in the ternary PV-X-plus system (PV2300:PV-A3:N1100), the introduction of a minor third component (N1100, 10wt.%), which exhibits a significantly larger surface energy mismatch relative to the major donor and acceptor, increases the likelihood of vertical compositional gradients. This is consistent with the  $\approx 10$  nm stratified top layer observed in the SLD profile (Figure 4c). Importantly, both binary (Figure S21, Supporting Information) and ternary (Figure 4a) blends exhibit symmetric  $J$ - $V$  characteristics at these thin PAL thicknesses for each stack, regardless of the illumination direction, indicating that the  $\approx 10$  nm top layer in the ternary system does not impact the  $J$ - $V$  symmetry. However, despite this symmetry, the binary system yields lower device performance compared to the ternary blend (Table S1, Supporting Information).

As the PV-X-plus system yields a largely homogeneous vertical phase distribution, one approach to induce vertical stratification is by increasing the concentration of the PAL solution. Upon increasing the concentration in both binary and ternary systems, we observe clear vertical stratification, with a  $\approx 70$ – $80$  nm top-

layer enrichment in  $\approx 250$  nm thick films (Figure S22, Supporting Information). This suggests that increasing solution concentration, and thereby film thickness, can promote vertical stratification by extending drying time, allowing more time for component redistribution. Additional factors such as differences in diffusion rates and solution-state aggregation may also contribute to this effect. While the influence of thickness-induced stratification is interesting, it lies beyond the primary scope of this study.

Although vertical stratification is influenced by a complex interplay of factors, our results suggest that the relatively homogeneous vertical phase distribution observed in the PV-X-plus ternary system arises from the good miscibility between the major donor-acceptor pair, the limited content of the minor third component, and possibly the solution-state behavior that leads to a characteristic thickness. Together, these factors contribute to the optimized performance of the IOPV device.

### 3. Conclusion

In this study, we showcase a failure issue in the industrially compatible symmetric lamination of OPVs, an issue that is not necessarily a problem for lab-scale devices and hence often goes unrecognized. We emphasize that certain successful photoactive layer blends, such as fullerene-based PBTZT-stat-BDTP:PC<sub>61</sub>BM and NFA-based PM6:IO-4Cl optimized for indoor applications, face significant limitations when evaluated in a scalable laminated semitransparent OPV device structure. Specifically, these blends exhibit reduced performance, particularly in  $J_{sc}$ , under anode illumination compared to cathode illumination. Experimental and simulation results indicate that vertical stratification within the photoactive layer, manifested as a polymer-rich region at the lamination interface of the cathode half-cell, is the root cause of this observed performance asymmetry. Based on these findings, we propose a model to explain the mechanism behind the  $J$ - $V$  asymmetry in these devices. During anode illumination, the reduced electron extraction results from the inhomogeneous vertical distribution within thick photoactive layers, where donor polymer enrichment at the lamination interface blocks the electron extraction process. Our findings highlight the complexity of vertical stratification, influenced by thermodynamic and kinetic factors. We further demonstrate that this phenomenon can be optimized for specific systems. Ultimately, the choice between achieving high performance or balanced cathode/anode performance will depend on specific application requirements. Through our exploration of various photoactive layer blends, we identified the commercially available ternary PV-X-plus PAL system, which delivers high and balanced performance owing to its nearly homogeneous vertical phase distribution in laminated device structures processed in ambient air, making it a compatible option for industrial applications.

### 4. Experimental Section

**Materials and Solution Preparation:** PBTZT-stat-BDTP polymer and PV-X-plus solution were obtained from Raynergy Tek and [6,6]-phenyl-C<sub>61</sub>-butyric acid methyl ester PC<sub>61</sub>BM was purchased from NanoC.

Poly[(2,6-(4,8-bis(5-(2-ethylhexyl-3-fluoro)thiophene-2-yl)-benzo[1,2-b:4,5-b']dithiophene))-alt-(5,5-(1',3'-di-2-thienyl-5',7'-bis(2-ethylhexyl)benzo[1',2'-c:4',5'-c']dithiophene-4,8-dione)] (PM6) with

$M_w$  of 102 kDa and  $M_n$  42 kDa and 3,9-bis[5,6-dichloro-1H-indene-1,3(2H)dione]-5,5,11,11-tetrakis(4-hexylphenyl)-dithieno[2,3-d:2',3'-d']-s-indaceno[1,2-b:5,6-b']dithiophene (IO-4Cl), 3,9-bis(2-methylene-((3-(1,1-dicyanomethylene)-6,7-difluoro)-indanone))-5,5,11,11-tetrakis(4-hexylphenyl)-dithieno[2,3-d:2',3'-d']-s-indaceno[1,2-b:5,6-b']dithiophene (IT-4F) were purchased from Solarmer. O-xylene, 1-Methylnaphthalene, and chlorobenzene (CB) were obtained from Sigma-Aldrich and used as received. Commercial ETL ink formulations containing  $\text{SnO}_2$  were purchased from Avantama and utilized following a 10 min horn sonication.

The pristine PEDOT:PSS (Clevious PH1000) from Heraeus GmbH was mixed with ethylene glycol (EG) from Sigma Aldrich and Capstone FS-30 surfactant (Dupont) in a volume ratio of 93.5:6:0.5 (PH1000:EG:FS-30) and further diluted in deionized water in a 2:1 ratio (v.v. ink:water). 125  $\mu\text{m}$  heat-stabilized polyethylene terephthalate (PET) Melinex ST505 (Tekra) was used as a substrate.

**Device Fabrication and Electrical Characterization:** Fabrication of laminated OPV devices began from slot-die coating (Solar X3, FOM Technologies) PEDOT:PSS electrodes (both cathode and anode electrode) on the PET substrate in air, followed by heating at 130 °C for 15 min. The cathode side of the device was processed by spin-coating  $\text{SnO}_2$  on PEDOT:PSS electrode and annealing at 115 °C for 2 min in the glovebox followed by spin-coating PALs and thermal annealing in the glovebox. The anode side of the device was processed by spin-coating PAL on PEDOT:PSS electrode and thermal annealing in the glovebox. PBTZT-stat-BDTP:PC<sub>61</sub>BM (1:1.5, w/w) blend was prepared in o-xylene:methylnaphthalene (85:15, v.v.) at 45 g L<sup>-1</sup> total concentration and spin-coated at 2000 rpm followed by thermal annealing at 80 °C for 2 min. PM6 and IO-4Cl were blended in 1:1.5 ratio (w/w) in CB (25 g L<sup>-1</sup> total concentration), spin-coated at 2000 rpm and thermally annealed at 80 °C for 2 min. PV-X-plus ink solution was used as received, then spin-coated at 600 rpm followed by annealing at 80 °C for 2 min.

The anode stack was pre-patterned using a scalpel to isolate three active areas per substrate. The active area is susceptible to subjective errors within a range of  $\pm 0.05 \text{ cm}^2$ . Subsequently, the cathode and anode stacks were laminated in the glovebox using a roll laminator (GSS DH-650S Graphical Solutions Scandinavia AB) with a roll temperature set at 115 °C and a force of  $\approx 50 \text{ N}$  (measured with a force sensor FlexiForce A201, Tekscan). Following the lamination, the devices were sandwiched between two glass slides to provide mechanical support for easier handling. Furthermore, silver paint (Agar AGG302) was applied to the exposed PEDOT:PSS contacts. Notably, the devices were not encapsulated.

**Electrical and Optical Characterization:** The  $J$ - $V$  curves of devices were measured by using a Keithley 2400 Source Meter under LED irradiation at a temperature ranging from 20–25 °C. The LED source's emission spectra and irradiance (refer to Figure S1 Supporting Information) were obtained using a high-precision fiber optics spectrometer (QE-Pro, Ocean Optics) and a Hamamatsu silicon photodiode S1133-01. Upon integration of the corresponding emission spectrum obtained<sup>[37]</sup> from the specific device location, the illuminance, power density, and current density were calculated as 500 lux, 152.17  $\mu\text{W cm}^{-2}$ , and 69  $\mu\text{A cm}^{-2}$ , respectively.

The EQE was obtained by using the Spectral Response Measurement System QE-R3011 (Enli Technology Co., Ltd).

**Temperature-Dependent  $V_{OC}$  Measurements:** Temperature-dependent  $J$ - $V$  measurements were conducted using a helium cryostat capable of cooling the device down to 10 K, with temperature control achieved through a Lakeshore temperature controller (model-335). The device was illuminated using a stable white light LED from Thorlabs (model-MBB1L3) at an intensity equivalent to 1 Sun, with varying intensities achieved using a neutral density filter (Thorlabs). The  $J$ - $V$  characteristics were measured at different temperatures and light intensities using a Keithley 2400 source meter. From these measurements, the open-circuit voltage  $V_{OC}$  was extracted and plotted as a function of temperature (Table S3, Supporting Information). A linear fit applied to the  $V_{OC}$ - $T$  graph was used to determine the effective bandgap  $E_{G,BHJ}$  of the photoactive layer. The  $E_{G,BHJ}$  value was used for electrical simulations.

Variable angle spectroscopic ellipsometry (VASE) was measured with a dual rotating compensator ellipsometer (J. A. Woollam, Co., Inc.) in the range 5–75° with step 10°. The optical constants of the spin-coated layers

on Si/SiO<sub>x</sub> substrates were modeled using the software CompleteEase (J. A. Woollam, Co., Inc.) with the B-Spline method. Both the active layer and pristine polymer thin films exhibited anisotropic behavior; therefore, both ordinary and extraordinary refractive indices were extracted. For optical simulations, only the ordinary refractive index values were used, as they represent the in-plane optical properties that dominate the light interaction in thin-film devices under normal incidence.

**X-Ray Reflectivity:** The XRR measurements were conducted using a high-resolution reflectometer equipped with a Cu  $K\alpha$  radiation source ( $\lambda = 1.54 \text{ \AA}$ ). The incident beam was conditioned using a Göbel mirror with a 1/32-degree slit and a 2 mm mask as part of the incidence optics, ensuring precise collimation and minimizing angular divergence for enhanced resolution. Additionally, a parallel beam collimator with a parallel beam collimator slit was used in the diffracted beam optics to further optimize beam quality. Data acquisition was performed over an angular range from 0 to 4 degrees, capturing the critical angle and multiple Kissig fringes to obtain layer thicknesses, interface roughness, and density contrasts using fits. The obtained reflectivity profiles were fitted using GenX 3 software,<sup>[26]</sup> enabling modeling and extraction of structural parameters for samples.

**Neutron Reflectivity:** Angular and energy-dispersive NR experiments were conducted at the AMOR reflectometer located at SINQ (Paul Scherrer Institut). The density depth profiles were measured on the angle- and energy-dispersive neutron reflectometer Amor<sup>[38]</sup> at PSI, Switzerland. On this instrument, the combination of time-of-flight reflectometry with a divergent beam focused to the sample allows for fast measurements in cases where no strong diffuse or off-specular scattering is expected. The respective ranges for the wavelength and the incident angle were 3 to 12.5 Å and 0.5 to 2.0°, which corresponds to a  $q_z$  range from 0.005 to 0.1 Å<sup>-1</sup>. The incident and final angles are deduced using a high-resolution position-sensitive detector.<sup>[39]</sup> The measurement time per sample (area 20 × 20 mm<sup>2</sup>) was 30 min. All reflectivity measurements were analyzed by using GenX 3.<sup>[26]</sup>

**Time-Of-Flight Secondary Ion Mass Spectroscopy:** Element depth profiles were obtained with a time-of-flight secondary ion mass spectrometer (ToF-SIMS V system, ION-TOF). The primary beam was 25 keV Bi<sup>3+</sup> with a total current of 0.43 pA and a raster size of 50 × 50  $\mu\text{m}^2$ . Cs<sup>+</sup> ions were used with 1000 eV ion energy, 40 nA pulse current on a 400 × 400  $\mu\text{m}^2$  raster size to bombard and etch the film.

**Contact Angle:** The contact angles were measured using CAM200 Goniometer at room temperature. Liquid droplets of deionized water, ethylene glycol, and diiodomethane were dropped onto the substrate with films using a precision syringe. The droplet's profile was captured immediately after deposition using a high-resolution camera. The contact angles of various films were used to calculate the surface energy values using two methods, Owens-Wendt and Fowkes methods.

**Fowkes Method:**

$$\frac{\gamma_l (\cos \theta + 1)}{2} = (\gamma_s^d)^{\frac{1}{2}} (\gamma_s^d)^{\frac{1}{2}} + (\gamma_s^p)^{\frac{1}{2}} (\gamma_s^p)^{\frac{1}{2}} \quad (1)$$

where  $\gamma_l^d$  and  $\gamma_l^p$  represent the dispersive and polar components of the liquid, and  $\gamma_s^d$  and  $\gamma_s^p$  are the corresponding components for the solid.

First, a nonpolar aprotic liquid, as diiodomethane, is used to determine the dispersive component of solid's surface energy ( $\gamma_s^d$ ) based on the given equation. Next, a polar protic liquid, such as water, is tested. Using the previously attained  $\gamma_s^d$ , the polar component of the solid's surface energy ( $\gamma_s^p$ ) is then calculated using the same calculation.

The total surface energy is the sum of the dispersive and polar components:

$$\gamma_s = \gamma_s^d + \gamma_s^p \quad (2)$$

**Owens-Wendt Method:** The surface energy at the solid-liquid interface ( $\gamma_{sl}$ ) is expressed as:

$$\gamma_{sl} = \gamma_s + \gamma_l - 2 \left( \gamma_s^d \gamma_l^d \right)^{\frac{1}{2}} - 2 \left( \gamma_s^p \gamma_l^p \right)^{\frac{1}{2}} \quad (3)$$

The equation for contact angle ( $\theta$ ) measurement is:

$$\frac{\gamma_l (\cos\theta + 1)}{2(\gamma_l^d)^{\frac{1}{2}}} = (\gamma_s^p)^{\frac{1}{2}} \frac{(\gamma_l^p)^{\frac{1}{2}}}{(\gamma_l^d)^{\frac{1}{2}}} + (\gamma_s^d)^{\frac{1}{2}} \quad (4)$$

Since the polar and dispersive components of the liquid's surface energy are known, plotting the left-hand side of this equation against  $(\gamma_l^p)^{\frac{1}{2}} / (\gamma_l^d)^{\frac{1}{2}}$  will result in a linear relationship. From this linear plot,  $\gamma_s^p$  can be obtained as the square of the slope and  $\gamma_s^d$  as the square of the y-intercept.

**Optical Simulations:** The charge generation profiles for the two cases, i.e., light impinging either from the cathode or the anode side were determined using optical simulations based on the transfer matrix approach. For this, the optical coefficients (refractive index (n) and extinction coefficients (k) values) of each material were determined from variable angle spectroscopic ellipsometry measurements of corresponding films on Si substrate.

**Electrical Simulations:** The electrical drift-diffusion simulations were carried out with Sentaurus TCAD.<sup>[40]</sup> The standard parameter set is listed below. Bimolecular recombination in the absorber and surface recombination are the loss mechanisms. However, due to the large band offsets between absorber and ETL and HTL, respectively, the latter can be neglected. The electrical parameters are given in Table S3 (Supporting Information).

**Statistical Analysis:** All experiments were performed with a minimum of three independent samples ( $n = 3$ ) unless otherwise stated. The statistical comparison of PV device performance for the laminated IOPV devices is given in Figure S23 (Supporting Information).

## Supporting Information

Supporting Information is available from the Wiley Online Library or from the author.

## Acknowledgements

The authors acknowledge the beamline on the neutron reflectometer Amor located at the neutron spallation source SINQ, Paul Scherrer Institute, Villigen, Switzerland; G.B., J.B., and F.G. acknowledge the Swedish Foundation for Strategic Research (SSF) (No. ID20-0105). A.Z. acknowledges the Royal Academy of Sciences Physics grant, PH2022-0029. F.E. acknowledge Swedish Research Council, VR, 2019-04837\_VR. O.I. and F.G. are Wallenberg Scholars.

## Conflict of Interest

Jonas Bergqvist, Thomas Österberg, and Olle Inganäs are co-founders of Epishine AB, which develops and manufactures organic photovoltaic devices for light energy harvesting.

## Data Availability Statement

The data that support the findings of this study are available from the corresponding author upon reasonable request.

## Keywords

indoor photovoltaics, lamination, organic photovoltaics, reflectivity, semi-transparency, solution processing, vertical stratification

Received: January 31, 2025

Revised: May 23, 2025

Published online:

- [1] M. Li, F. Igbari, Z. K. Wang, L. S. Liao, *Adv. Energy Mater.* **2020**, *10*, 200641.
- [2] I. Mathews, S. N. Kantareddy, T. Buonassisi, I. M. Peters, *Joule* **2019**, *3*, 1415.
- [3] V. Pecunia, L. G. Occhipinti, R. L. Z. Hoyer, *Adv. Energy Mater.* **2021**, *11*, 2100698.
- [4] B. Li, B. Hou, G. A. J. Amaratunga, *InfoMat* **2021**, *3*, 445.
- [5] Y. Cui, L. Hong, J. Hou, *ACS Appl. Mater. Interfaces* **2020**, *12*, 38815.
- [6] H. S. Ryu, S. Y. Park, T. H. Lee, J. Y. Kim, H. Y. Woo, *Nanoscale* **2020**, *12*, 5792.
- [7] Z. Hu, J. Wang, X. Ma, J. Gao, C. Xu, K. Yang, Z. Wang, J. Zhang, F. Zhang, *Nano Energy* **2020**, *78*, 105376.
- [8] M. F. Müller, M. Freunek, L. M. Reindl, *IEEE J. Photovolt.* **2013**, *3*, 59.
- [9] Y. Cui, Y. Wang, J. Bergqvist, H. Yao, Y. Xu, B. Gao, C. Yang, S. Zhang, O. Inganäs, F. Gao, J. Hou, *Nat. Energy* **2019**, *4*, 768.
- [10] F. Bai, J. Zhang, A. Zeng, H. Zhao, K. Duan, H. Yu, K. Cheng, G. Chai, Y. Chen, J. Liang, W. Ma, H. Yan, *Joule* **2021**, *5*, 1231.
- [11] B. Zhang, F. Yang, Y. Li, *Small Sci.* **2023**, *3*, 2300004.
- [12] G. Bernardo, T. Lopes, D. G. Lidzey, A. Mendes, *Adv. Energy Mater.* **2021**, *11*, 2100342.
- [13] J. Bergqvist, T. Österberg, A. Melianas, L. Ever Aguirre, Z. Tang, W. Cai, Z. Ma, M. Kemerink, D. Gedefaw, M. R. Andersson, O. Inganäs, *npj Flexible Electron.* **2018**, *2*, <https://doi.org/10.1038/s41528-017-0017-6>
- [14] X. Rodríguez-Martínez, P. Hartnagel, S. Riera-Galindo, G. Beket, T. Österberg, F. Gao, T. Kirchartz, O. Inganäs, *Adv. Funct. Mater.* **2023**, *33*, 2301192.
- [15] M. C. Scharber, N. S. Sariciftci, *Prog. Polym. Sci.* **2013**, *38*, 1929.
- [16] C. J. Brabec, J. R. Durrant, *MRS Bull.* **2008**, *33*, 670.
- [17] E. M. Herzig, F. Gao, J. Bergqvist, M. A. Loi, S. B. Meier, *Joule* **2024**, *8*, 2171.
- [18] M. Moser, A. Wadsworth, N. Gasparini, I. McCulloch, *Adv. Energy Mater.* **2021**, *11*, 2100056.
- [19] N. Camaioni, C. Carbonera, L. Ciammaruchi, G. Corso, J. Mwaure, R. Po, F. Tinti, *Adv. Mater.* **2023**, *35*, 2210146.
- [20] H. Zhao, J. Xue, H. Wu, B. Lin, Y. Cai, K. Zhou, D. Yun, Z. Tang, W. Ma, *Adv. Funct. Mater.* **2023**, *33*, 2210534.
- [21] C.-Y. Liao, Y.-T. Hsiao, K.-W. Tsai, N.-W. Teng, W.-L. Li, J.-L. Wu, J.-C. Kao, C.-C. Lee, C.-M. Yang, H.-S. Tan, K.-H. Chung, Y.-M. Chang, *Sol. RRL* **2021**, *5*, 2000749.
- [22] S. Berny, N. Blouin, A. Distler, H. J. Egelhaaf, M. Krompiec, A. Lohr, O. R. Lozman, G. E. Morse, L. Nanson, A. Pron, T. Saueremann, N. Seidler, S. Tierney, P. Tiwana, M. Wagner, H. Wilson, *Adv. Sci.* **2015**, *3*, 1500342.
- [23] N. B. Kotadiya, A. Mondal, P. W. M. Blom, D. Andrienko, G. J. A. H. Wetzelaer, *Nat. Mater.* **2019**, *18*, 1182.
- [24] J. Guo, Y. Wu, R. Sun, W. Wang, J. Guo, Q. Wu, X. Tang, C. Sun, Z. Luo, K. Chang, Z. Zhang, J. Yuan, T. Li, W. Tang, E. Zhou, Z. Xiao, L. Ding, Y. Zou, X. Zhan, C. Yang, Z. Li, C. J. Brabec, Y. Li, J. Min, *J. Mater. Chem. A Mater* **2019**, *7*, 25088.
- [25] Y. Yan, X. Liu, T. Wang, *Adv. Mater.* **2017**, *29*, 1601674.
- [26] A. Glavic, M. Björck, *J. Appl. Crystallogr.* **2022**, *55*, 1063.
- [27] S. Yoon, N. Schopp, D. G. Choi, H. Wakidi, K. Ding, H. Ade, H. Vezin, G. N. Manjunatha Reddy, T.-Q. Nguyen, *Adv. Funct. Mater.* **2024**, *34*, 2308618.
- [28] A. Zdziennicka, K. Szymczyk, J. Krawczyk, B. Jańczuk, *Appl. Surf. Sci.* **2017**, *405*, 88.
- [29] D. Cwikel, Q. Zhao, C. Liu, X. Su, A. Marmur, *Langmuir* **2010**, *26*, 15289.
- [30] S. Shalel-Levanon, A. Marmur, *J. Colloid Interface Sci.* **2003**, *262*, 489.
- [31] Q. Li, L.-M. Wang, S. Liu, X. Zhan, T. Zhu, Z. Cao, H. Lai, J. Zhao, Y. Cai, W. Xie, F. Huang, *ACS Appl. Mater. Interfaces* **2019**, *11*, 45979.

- [32] Q. Li, L.-M. Wang, S. Liu, L. Guo, S. Dong, G. Ma, Z. Cao, X. Zhan, X. Gu, T. Zhu, Y.-P. Cai, F. Huang, *ACS Energy Lett.* **2020**, *5*, 3637.
- [33] W. M. Haynes, *CRC Handbook of Chemistry and Physics*, 95th ed, CRC Press, Boca Raton, FL **2014**.
- [34] Q. Li, X. Liao, Y. Sun, Y. Xu, S. Liu, L. M. Wang, Z. Cao, X. Zhan, T. Zhu, B. Xiao, Y. P. Cai, F. Huang, *Small* **2023**, *20*, 2308165.
- [35] A. A. A. Torimtubun, M. Méndez, E. Moustafa, J. Pallarès, E. Palomares, L. F. Marsal, *Sol. RRL* **2023**, *7*, 2300228.
- [36] S. Wu, *J. Polym. Sci.* **1971**, *34*, 19.
- [37] Y. Cui, L. Hong, T. Zhang, H. Meng, H. Yan, F. Gao, J. Hou, *Joule* **2021**, *5*, 1016.
- [38] J. Stahn, A. Glavic, *Nucl. Instrum. Methods Phys. Res. A* **2016**, *821*, 44.
- [39] F. Piscitelli, F. Ghazi Moradi, F. S. Alves, M. J. Christensen, J. Hrivnak, A. Johansson, K. Fissum, C. C. Lai, A. Monera Martinez, D. Pfeiffer, E. Shahu, J. Stahn, P. O. Svensson, *J. Instrum.* **2014**, *19*, P05010.
- [40] Sentaurus TCAD: release U-2022.12-SP1 **2022**.